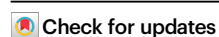


Septin5 deletion enhances β -cell exocytosis by releasing microtubule-tethered insulin granules onto plasma membrane

Received: 22 February 2024

Accepted: 19 February 2025

Published online: 19 March 2025



Li Xie^{1,2,6} , Fei Kang^{1,2,6} , Tairan Qin^{1,2}, Youhou Kang^{1,2}, Tao Liang^{1,2}, Huanli Xie^{1,2}, Carol D. Froese³, Hong Xie³, Aaron Au^{4,5}, Christopher M. Yip^{4,5}, William S. Trimble³ & Herbert Y. Gaisano^{1,2} 

Septin5 interacts with SNARE proteins to regulate exocytosis in neurons, but its role in pancreatic β -cells is unknown. Here, we report that Septin5 is abundant in rodent and human β -cells, deletion of which dramatically enhances biphasic glucose-stimulated insulin secretion, including in type 2 diabetes (T2D). Super-resolution imaging shows that Septin5 is preferentially assembled in microtubule-plasma membrane contact sites in a microtubule-dependent manner, which provides discrete harbor for secretory granule anchoring. By decreasing the stability of the cortical microtubule meshwork, Septin5 depletion increases insulin granule dynamics and access to the plasma membrane. Analysis of spatiotemporal coupling of fusion events and localized Ca^{2+} influx through L-type Ca^{2+} channels show that Septin5 depletion increases releasable granule pool clustering on Ca^{2+} channels, previously shown to be impaired in T2D, thus rectifying this T2D defect. Hence, inhibition of Septin5 can improve insulin secretion.

Septins are a highly conserved family of GTP-binding proteins that were originally identified as filamentous proteins required for cytokinesis in budding yeast¹ and have been implicated in a diverse array of cellular functions, including cell division, secretion, migration, and ciliogenesis². Four yeast septins (Cdc3, Cdc10, Cdc11 and Cdc12) were originally identified in a temperature-sensitive screen for cell division cycle defects³. In mammals, there are 13 septins (Septin1-12 and Septin14) that fall into four groups with sequence similarity to the four yeast septins⁴. Some of these, including Septin2, Septin11, Septin7, and Septin9, have been shown to be involved in cytokinesis⁵⁻⁷. Similar to actin and tubulin, septins are able to polymerize into filaments. Septin filaments are thought to act as a macromolecular scaffold, recruiting proteins to particular cellular locations in order to mediate specific functions⁸. For instance, mammalian septins

have been shown to localize to the ingressing furrow in dividing cells where Septin2 binds to non-muscle myosin II to promote its activation⁶. In addition, septin filaments also tend to reorganize into ring structures that have been shown to act as diffusion barrier, preventing the lateral movement of membrane and peripheral proteins⁸⁻¹⁰.

Septin5, a septin family member formerly called cell division control related protein 1 (CDCrel-1), is encoded in the 200 kb region and is abundantly expressed in the developing and adult brains of mice and humans¹¹⁻¹³. Septin5 is expressed in presynaptic terminals¹² and exerts negative regulatory control over neurotransmitter release by binding to the Syntaxin SNARE (soluble N-ethylmaleimide-sensitive factor attachment protein receptor) protein¹⁴ and showed that it may play a role in regulating SNARE function^{14,15}. Specifically, Septin5 was shown to associate with vesicles and membranes through its

¹Department of Medicine, Temerty Faculty of Medicine, University of Toronto, Toronto, ON, Canada. ²Toronto General Hospital Research Institute, University Health Network, Toronto, ON, Canada. ³The program in Cell Biology, Department of Biochemistry, Hospital for Sick Children, University of Toronto, Toronto, ON, Canada. ⁴Institute of Biomedical Engineering, University of Toronto, Toronto, ON, Canada. ⁵Donnelly Centre for Cellular & Biomolecular Research, University of Toronto, Toronto, ON, Canada. ⁶These authors contributed equally: Li Xie, Fei Kang. ✉ e-mail: li.xie@utoronto.ca; fei.kang@uhn.ca; herbert.gaisano@utoronto.ca

interaction with the SNARE domain of syntaxin 1A and the 7S SNARE complex, and appears to inhibit exocytosis, possibly by regulating vesicle targeting and/or fusion events^{14,16}.

It was reported that Septin5 gene is expressed in normal and neoplastic human endocrine pancreas¹⁷, and overexpression of Septin5 inhibited the secretion of storage granules from an insulin-secreting cell line¹⁴. In this work, we comprehensively assess Septin5 function in regulating β -cell insulin secretory granule (SG) exocytosis using Septin5 knockout (KO) mice¹⁸, non-obese T2D Goto-Kakizaki (GK) rats known to closely mimic non-obese human T2D¹⁹, and human donor islets, and show that deletion of Septin5 enhances biphasic glucose-stimulated insulin secretion (GSIS) and improves glucose homeostasis. Further, we demonstrate the subcellular localization of Septin5 at microtubule-plasma membrane (MT-PM) contact sites, deletion of which results in MT remodeling upon glucose stimulation and consequently releases SGs to dock onto calcium channels on the PM, thereby increasing the size of the pool of primed SGs available for exocytosis; which would be highly desirable in rescuing the insulin secretory deficiency in T2D.

Results

Septin5 is abundant in pancreatic islet β -cells

Septin5 is present in rat, human and rat insulinoma cell line INS 832/13 (Fig. 1a). Whereas exocytotic SNARE protein levels are generally reduced in T2D GK rat and T2D human islets as we and co-workers have previously reported¹⁹, islet Septin5 levels were similar between normal (Wistar rat, human) and the T2D islets, as are actin and tubulin used as controls (Fig. 1b, c). Within the human and mouse islet, we observed that Septin5 is abundantly expressed in all cell-types of the islets, particularly, in β -cells (Fig. 1d, Supplementary Fig. 1a). When examining the endogenous expression of Septin5 with immunostaining in both dispersed human β -cell and islets from six non-diabetic and three T2D donors (donor information see Supplementary Information), we found that all β -cells express Septin5 with variation in level rather than in an all-or-none manner, with uneven distribution of Septin5 at intracellular and intercellular levels (Fig. 1d, e), suggesting that the expression level of Septin5 in β -cells across an islet is heterogeneous. The abundant expression of Septin5 in β -cells suggested that Septin5 may be involved in regulating insulin secretion, which we pursued.

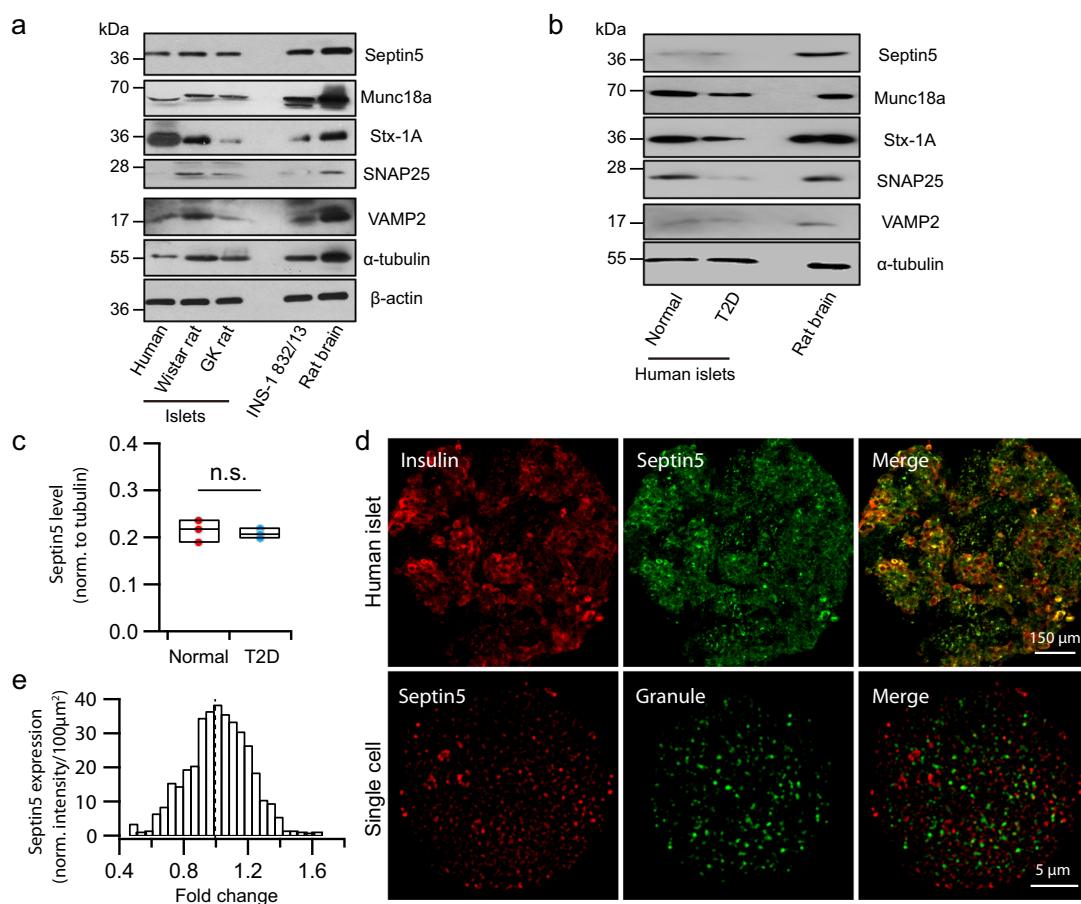


Fig. 1 | Septin5 is abundant in pancreatic islet β -cells. **a** Western blotting showing Septin5 is present in human and rodent islets. Rat insulinoma INS-1 is shown for comparison. **b** Western blotting showing Septin5 is present human islets, whose levels were not reduced in T2D human islets, as is also the case with GK rat islets in (a). SNARE proteins are reduced in both T2D human and GK islets (in (a)) compared to normal islets. **c** Quantification of band intensity (normalized to tubulin) in (b) showing similar expression level of Septin5 in human normal and T2D islets ($n = 3$ normal donors and 3 T2D donors). Statistical significance was assessed by a two-tailed Student's t -test (n.s., not significant). For boxplots, boxes indicate 25th and 75th percentiles, the lines within boxes mark medians, whiskers above and below

boxes indicate the 90th and 10th percentiles. **d** Lightning confocal images of human islet (top) and dispersed single β -cell (bottom) immunostained with Septin5 and insulin show Septin5 is abundant in pancreatic β -cells. A similar experiment was performed on mouse islets (Supplementary Fig. 1). **e** Quantification of endogenous Septin5 by immunostaining showing the heterogeneity of Septin5 expression in both dispersed human β -cells and intact islets from six non-diabetic and three T2D donors. Data are normalized to the average intensity. All the data shown are representative of at least 3 separate experiments. Source data are provided as a Source Data file.

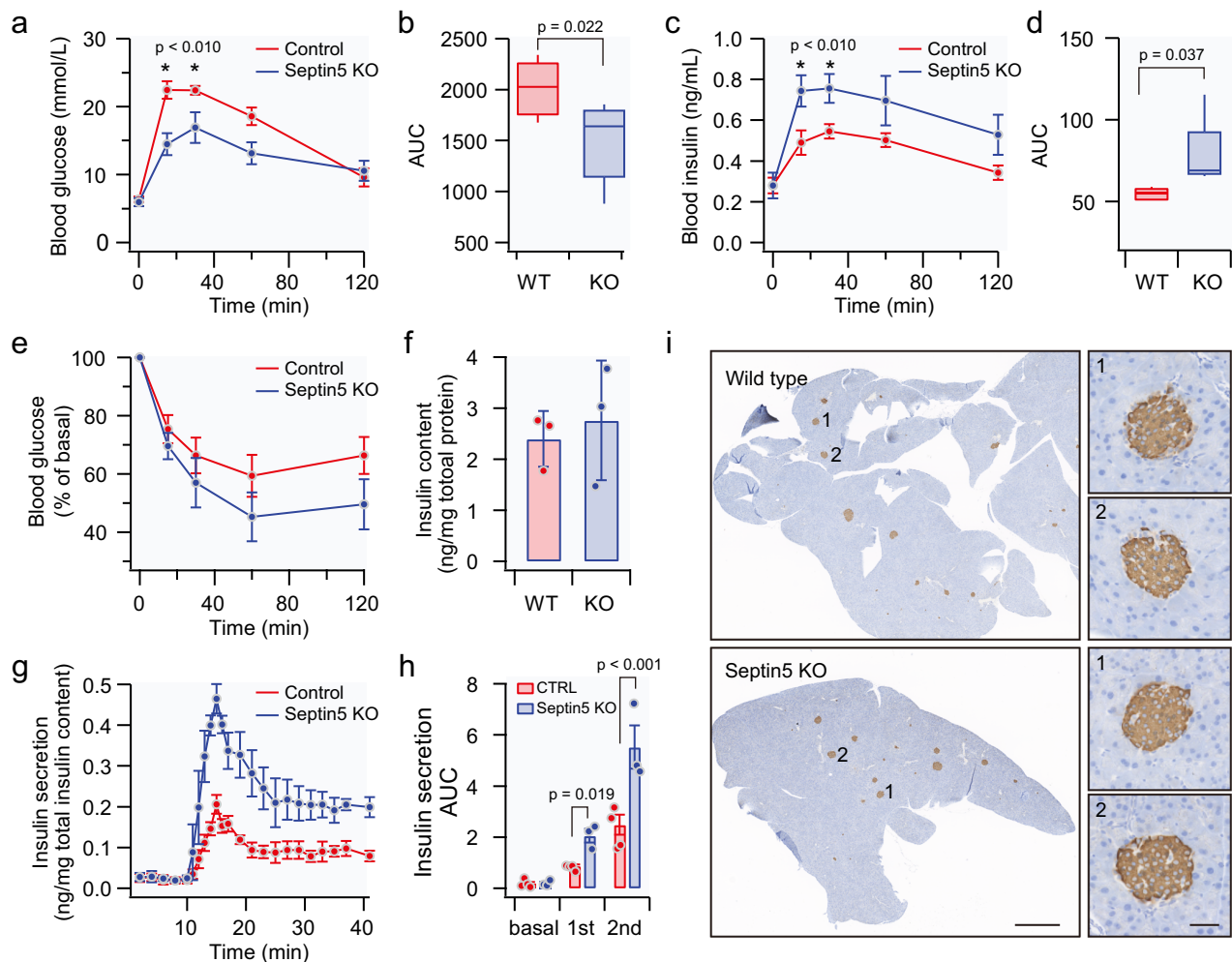


Fig. 2 | Septin5 KO mice have superior glucose tolerance as a result of higher biphasic GSIS. **a–d** IPGTTs were performed to assess blood glucose (**a**, **b**) and secreted insulin levels (**c**, **d**) and shown as AUC (area under the curve) analysis encompassing 120 min of the IPGTT for blood glucose (**b**) and insulin levels (**d**). $N = 5$ mice for each group, with summary graphs shown as mean \pm SEM. Septin5 deletion was first confirmed in isolated islets, which did not affect the total islet insulin content (Supplementary Fig. 2a). For boxplots, boxes indicate 25th and 75th percentiles, the lines within boxes mark medians, whiskers above and below boxes indicate the 90th and 10th percentiles. **e** Blood glucose levels during IPITT showing no significant difference ($n = 4$ for control, and 6 for Septin5 KO from three

biologically independent experiments). **f** Total insulin content is not affected in Septin5 KO mice. **g–h** Biphasic GSIS determined by islet perfusion assays (**g**) of WT vs Septin5 KO mice and the corresponding AUC analysis (**h**) for first phase (first 10 min) and second phase (next 20 min) GSIS. Summary graphs from 4 biologically independent experiments shown as mean \pm SEM. **i** Insulin-immunostained pancreatic sections. Septin5 KO does not alter the size, number and distribution of islets within the pancreas. Supplementary Fig. 2b, c shows the analysis for islet size and number. Scale bars, left, 1 mm, right, 100 μ m. Statistical significance was assessed by a two-tailed Student's *t*-test ($*p < 0.05$, the precise statistical results indicated in figures). Source data are provided as a Source Data file.

Mice lacking Septin5 exhibit superior glucose tolerance as a result of increased biphasic GSIS from pancreatic islets

We next assessed for glucose homeostasis and insulin secretion in our global Septin5-KO mouse¹⁸. Septin5 deletion was confirmed in total isolated islets, but the overall level of insulin was not affected (Supplementary Fig. 2a). Septin5 KO mice exhibited a superior glucose tolerance than WT mice evaluated by intraperitoneal glucose tolerance tests (IPGTT) (Fig. 2a, b). In fact, plasma insulin collected during IPGTT showed correspondingly higher insulin levels in Septin5-KO mice than WT mice (Fig. 2c, d). We then performed intraperitoneal insulin tolerance tests (IPITT) and found there was no significant effect on insulin sensitivity in Septin5-KO mice compared to WT mice (Fig. 2e, f). We isolated islets from these mice and conducted islet perfusion assays to assess physiologic biphasic GSIS (Fig. 2g). Area under the curve (AUC) analysis (Fig. 2h) showed that Septin5-KO islets exhibited increases of 137% in first-phase (Septin5-KO: 2.06 ± 0.27 ; WT: 0.87 ± 0.06) and 122%

in second-phase (Septin5-KO: 5.53 ± 0.85 ; WT: 2.49 ± 0.39) GSIS over WT islets. There was no difference in size, number and distribution of islets between Septin5-KO and WT mice (Fig. 2i, Supplementary Fig. 2b, c), indicating an increase in secretory capacity *per* Septin5-KO β -cell (see next).

Septin5 deletion in human islets increased biphasic GSIS by recruiting newcomer insulin SGs granules to PM to undergo exocytosis

We depleted Septin5 in human islets by ~81.9% (Fig. 3a, Supplementary Fig. 3a) using an adeno-Septin5 shRNA and conducted islet perfusion assays (Fig. 3b), which showed that Septin5 depletion increased first-phase GSIS by 46% (Septin5-KD: 7.05 ± 0.49 ; WT: 4.83 ± 0.37) and second-phase GSIS by 82% (Septin5-KD: 18.6 ± 1.81 ; WT: 10.2 ± 1.22 , Fig. 3c). We then assessed the population of insulin SGs that account for this increase in biphasic GSIS. To visualize the

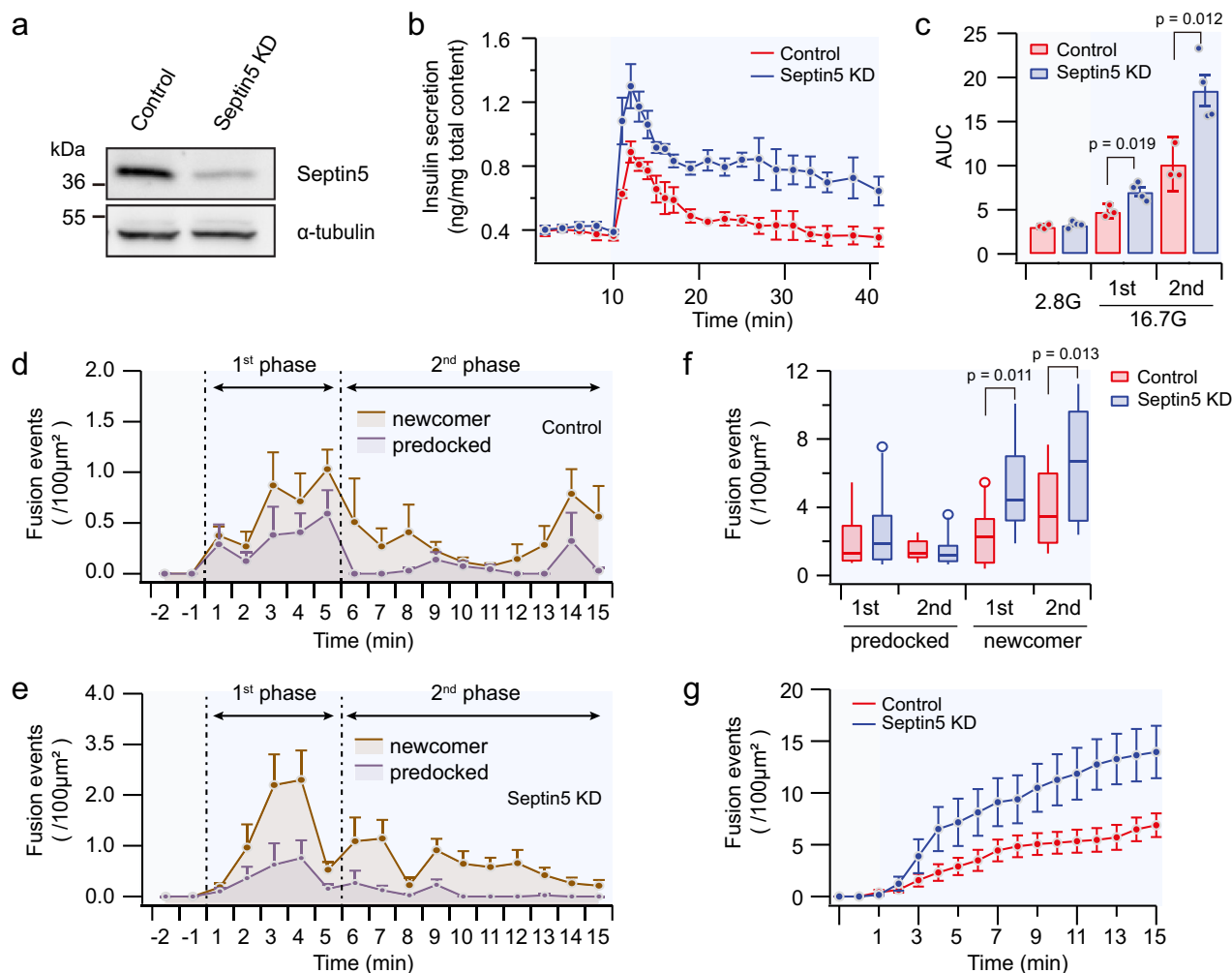


Fig. 3 | Septin5 depletion in human islets increases biphasic insulin secretion by increasing the exocytosis of newcomer insulin granules. **a** Western blotting showed that Septin5 level was 81.9% reduced compared to control (Ad-control) when human islets infected with Ad-Septin5 shRNA (Septin5 KD) ($n = 3$). Quantitative analysis of the experiments shown in Supplementary Fig. 3a. **b** Human islets perfusion assay showed that depletion of Septin5 in human islets increased both first- and second-phase GSIS. **c** AUC analysis of first-phase (10–20 min) and second-phase (21–41 min) GSIS. Basal secretion was not significantly affected. Plotted are the mean values of 4 biologically independent experiments, and bars represent SEM for (**b**, **c**). **d–g** TIRF imaging showed the fusion events in the first phase (first 5 min) and second phase (6–15 min) ($n = 10$ cells for each condition from 5 normal

donors. Supplementary Movie 1), expressed as mean \pm SEM. **f** The summary of fusion events with pre-docked and newcomer granules in first and second phase in both conditions. Pre-docked granules at basal (2.8 mM glucose) were not different between WT and Septin5 KO β -cells (Supplementary Fig. 3b, c). Boxes indicate 25th and 75th percentiles, the lines within boxes mark medians, whiskers above and below boxes indicate the 90th and 10th percentiles. **g** Normalized cumulative fusion events of SGs per unit area from control and Septin5 KD human β -cells. Statistical significance was assessed by a two-tailed Student's *t*-test ($p < 0.05$, the precise statistical results indicated in figures). Source data are provided as a Source Data file.

spatio-temporal mobilization of populations of SGs and single SG fusion dynamics, we employed time-lapse total internal reflection microscopy (TIRFM) to monitor exocytosis of SGs tagged with NPY-EGFP as described before^{20,21}. At basal 2.8 mM glucose, we seldom found spontaneous fusion events, with total docked SGs not different between WT and Septin5-KD cells (Supplementary Fig. 3b, c). When stimulated with 16.7 mM glucose, single SG fusion events were observed as flashes of fluorescence, which rapidly dissipated in a cloud-like diffusion pattern. We compared fusion events with pre-docked and newcomer granules in each minute between control and Septin5-KD cells (Fig. 3d, e, Supplementary Movie 1). Consistently, assessment of cumulative fusion events over time showed many more fusion events during the 15 min stimulation in Septin5-KD than in control β -cells (Fig. 3g), in which Septin5-KD increased both first-

and second-phase GSIS (Fig. 3f). In first-phase GSIS, pre-docked SGs accounted for $>50\%$ of exocytotic events in control cells, but there was no difference between control and Septin5-KD cells (Fig. 3f). The larger increase from Septin5-KD β -cells seems to be mainly attributed to a 128% increase in exocytosis of newcomer SGs (Septin5-KD: 5.2 ± 0.8 events/ $100\mu\text{m}^2$; WT: 2.3 ± 0.5 events/ $100\mu\text{m}^2$). Newcomer SGs, unlike pre-docked SGs, undergo minimal to no residence time at the PM before undergoing fusion²². Second phase GSIS is attributed almost entirely to newcomer SGs²², and here, the observed increase in second-phase GSIS from Septin5-KD β -cells was due to a large increase of 76% in newcomer SGs fusion (Septin5-KD: 6.7 ± 1.1 events/ $100\mu\text{m}^2$; WT: 3.8 ± 0.7 events/ $100\mu\text{m}^2$). These results indicate that Septin5 deletion mainly increases the exocytosis efficiency of newcomer SGs.

Septin5 assembles at MT-PM contact sites in a MT-dependent manner

Septins are filamentous GTP-binding proteins found to be associated with the synergistic MT and actin cytoskeleton²³. Septin5 has been classified into Septin2 group based on sequence similarity, whose members have been shown to associate with MT and affect MT organization and growth^{24–26}. To assess its dependence on the cytoskeleton, Septin5-regulated insulin secretion in human islets was further analyzed by pharmacological perturbations of MT and actin. β -cell secretion in response to glucose stimulus is regulated by stability of the MT network, destabilization of which leads to significant over-secretion, while hyper-stabilization greatly suppresses secretion^{27–30}. We found the Septin5-depletion induced over-secretion compared to control was eliminated by MT destabilizer nocodazole but remained constant by actin destabilizer latrunculin. Furthermore, MT stabilizer taxol caused major inhibition of GSIS from Septin5-depleted islets but seemed to also more mildly inhibited GSIS in WT control islets (Fig. 4a). Therefore, these results indicate that Septin5 associates with MT to modulate GSIS.

To examine the locations and relationship of Septin5, MT and SGs, we employed three-color labeling, including immunostaining with anti-Septin5-TxRed and anti-tubulin-Cy5 antibodies, and infected with Ad-NPY-EGFP to label insulin SGs; and then imaged by super-resolution structured illumination microscopy (SR-SIM). As shown in the depth-color encoded 3D SIM images, similar red (orange) color of Septin5 and MT overlap each other while connecting to granules with color shifting to the cell interior, well depicted in the enlarged boxed images (Fig. 4b, c; Supplementary Fig. 4 for one more representative β -cell), suggesting that Septin5 assembles at the contacts sites of cortical MT and PM, serving as harbors for granule anchoring. Given that the ultra-thin optical sectioning capability makes TIRF being considered as “gold standard” for investigating PM-related contact structure of adherent cells^{31–34}, the MT-PM contact sites where Septin5 assembled were visualized more clearly in the TIRF section images obtained by 3D SIM (Fig. 4c). Moreover, from observation of the localization of an estimated 30,000–45,000 insulin granules from ~80 human pancreatic β -cells, none of the granules was observed locating within the region of the contact sites. Given the fact that the size of granules varies from 50 nm to 500 nm³⁵, our observation above demonstrated that even the smallest granules are not able to enter the narrow apposition space of the MT-PM contact sites, suggesting that the apposition distance between MT and PM is less than 50 nm, which is generally in line with the reported 15–25 nm definition of contact sites³⁶. Therefore, the color-shifting depiction of the localization of anchored granules more into the cell interior makes sense. The cortical MT meshwork and anchoring of SGs to the MT-PM contact sites were not altered by Septin5 deletion (Fig. 4d and bottom optical section in Fig. 4e). On the other hand, although majority of filamentous MT disrupted as punctate (Supplementary Fig. 5a) after treatment with MT-depolymerizing nocodazole, Septin5 associated with PM can be still assembled at MT-PM contact sites the same as its location in the control (Fig. 4b, c). Conversely, actin-depolymerizing latrunculin did not alter the MT-PM contact sites (Supplementary Fig. 5b). Taken together, these super-resolution imaging results suggested that Septin5 assembles at MT-PM contact sites in a MT-dependent manner.

Septin5 depletion increase SGs mobility and its access to PM by regulating cortical MT stability

To understand how this particular component of the cytoskeleton, the cortical MT-associated GTP-binding protein Septin5, affects insulin granule behavior, specifically SG mobility and its access to PM, we performed a series of single-granule tracking and spatiotemporal averaging analyses using live-cell TIRF microscopy. Using trajectory sum of granules analysis, which reflects the pathway the SGs traveled after arriving at the PM, there were more SG dynamic movements in

Septin5-depleted β -cells than control β -cells during glucose stimulation (Fig. 5a, b). Comparing the histogram of single granule diffusion coefficients during glucose stimulation, the highly dynamic component (as indicated by asterisk) significantly increased in Septin5-KD compared to control β -cells, while the restricted SGs (the middle population as red fit-curve indicated) decreased correspondingly (Fig. 5c, d). Cortical MT controls SGs' access to PM, which on glucose stimulation would undergo depolymerization and reduce granule withdrawal to the cell interior, leading to release of SGs to docking sites^{27–29,37–39}. To visualize the movement of granules before fusion occurs at nanoscale, a scale beyond the resolution limit of the live fluorescence microscopy, we introduced an analysis method by spatially aligning and then temporal averaging of single fusion events to visualize the PM access of insulin SGs. To be specific, we spatially aligned the SG fusion events using their center coordinates with a window size of 9×9 pixels and temporally averaged the NPY-GFP signal during the 5-s preceding fusion pore opening⁴⁰. Ensemble average intensity revealed the PM region that SG “explored” before fusion. Apparently, SGs explored a larger area of the PM surface in Septin5-depleted cells before fusion occurred (Fig. 5e). We reasoned that the nanoscale density fluctuation of cortical meshwork would allow increased likelihood of granules to explore more PM surface and be captured by the fusion machinery. To evaluate the dynamics of cortical MT after glucose stimulation, we further assessed whether the MT-templated assembly of Septin5 at MT-PM contact sites plays a role in MT stability. We assessed the relative stability by immunostaining deetyrosinated alpha-tubulin (Glu-tubulin), a marker having been reported to indicate the stability of MT⁴¹. As shown by the ratio of Glu-tubulin to tubulin, Septin5 depletion decreased the MT stability after high glucose stimulation without markedly affecting the overall density of the tubulin meshwork, while no significant change was observed under basal condition, suggesting that the MT instability specifically induced by Septin5 depletion is dependent on glucose metabolism (Fig. 5f and Supplementary Fig. 6). Given the fact that increased motion and travel of SGs increases fusion probability⁴², these collective analyses suggested that Septin5 depletion increases granule fusion by remodeling the cortical MT meshwork and consequently facilitate SG access to PM fusion sites.

Septin5 depletion increases the number of granules that associate and fuse with higher efficiency on L-type Ca^{2+} channels

While it is known that Ca^{2+} entry through voltage-gated L-type Ca^{2+} channels is required for insulin granules exocytosis, insulin secretory granules actually cluster at and bind the L-type Ca^{2+} channels^{43–45} where they undergo exocytosis, and this association could be pathologically disrupted in T2D^{46,47}. To evaluate whether Septin5 could affect these processes, we mapped the spatial distribution of L-type Ca^{2+} channels using TIRFM by loading Fluo-5F, a fast-binding, low-affinity Ca^{2+} indicator as well as EGTA, a slow-binding but high-affinity Ca^{2+} chelator⁴⁷. Upon Ca^{2+} influx induced by membrane depolarization, the local fluorescence transients reflect the spatial distribution of L-type Ca^{2+} channels. Since moving to a docking receptor is the prerequisite for granule fusion, we asked whether the increased granule motion and travel region before fusion induced by Septin5 depletion increased the probability for granules to find a favorable location to cluster with L-type Ca^{2+} channels for subsequent fusion. To maximize Ca^{2+} influx to deplete all readily releasable granules in close apposition to L-type Ca^{2+} channels but minimizing the contribution from distant cytoplasmic Ca^{2+} activity, high K^+ at 75 mM has been used to steeply depolarize and rapidly open voltage-gated Ca^{2+} channels that would deplete by exocytotic fusion of secretion-ready insulin granules^{47,48}. On the other hand, high concentration of Ca^{2+} chelator EGTA together with short pulses of high K^+ for 1 s every 10 s restricts Ca^{2+} influx in microdomains (a radius of ~100 nm), without contribution to the global cytoplasm by hampering Ca^{2+} diffusion^{47,49,50}. We compared the fusion events

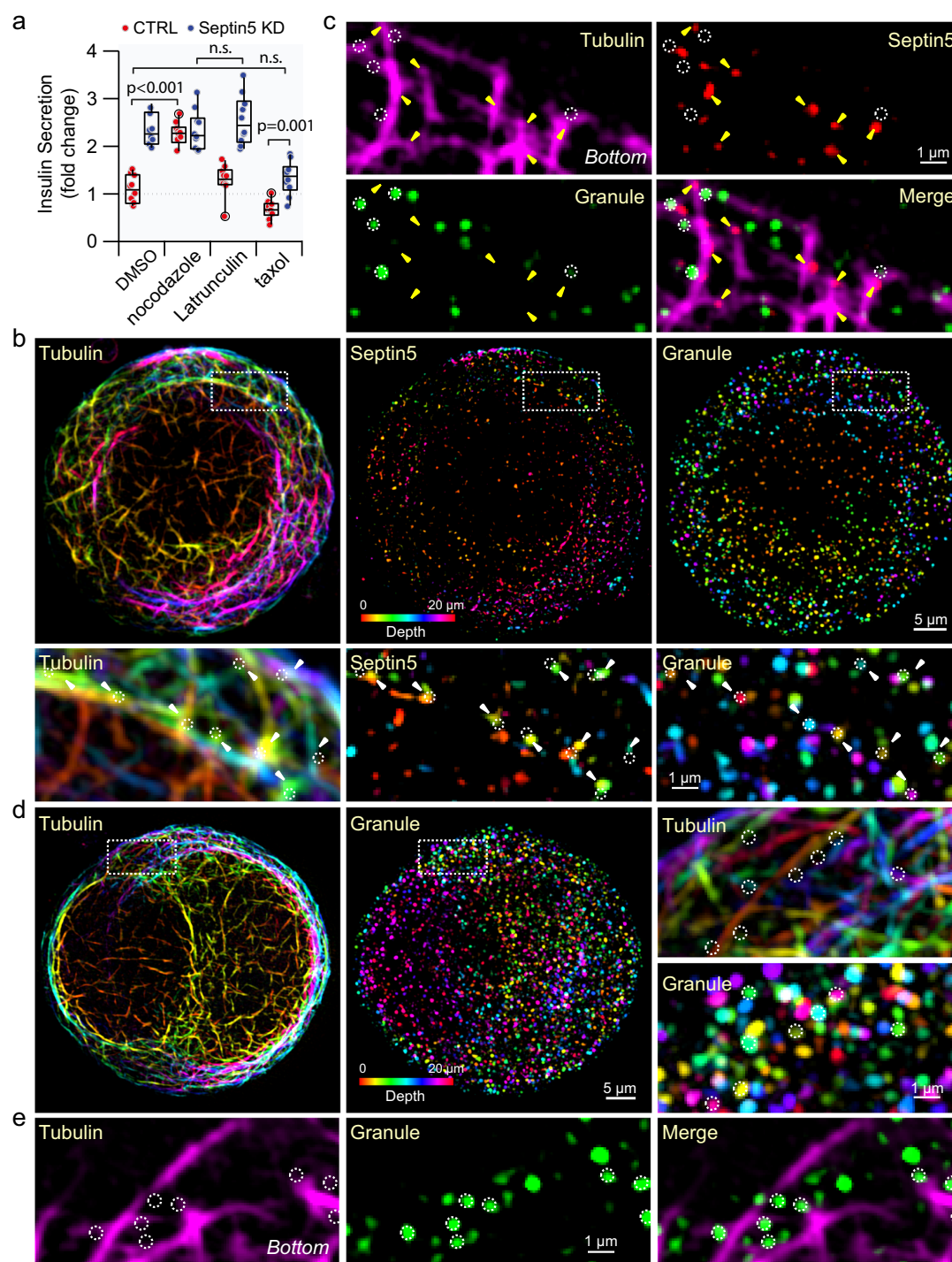


Fig. 4 | Septin5 assembles at MT-PM contact sites in a MT-dependent manner. **a** Septin5 depletion in human islets increases GSIS by affecting MT rather than actin microfilaments. Insulin secretion over 30 min upon 16.7 mM glucose stimulation as measured by ELISA. Human islets after two-round infection with control or Ad-Septin5 shRNA were incubated with DMSO, nocodazole, latrunculin or taxol. Data are presented as box-plots where the central line represents the median value, the box shows percentiles 25–75 and the whiskers include the most extreme values (two-tailed Student's t -test, n.s. denotes not significant). **b–e** Representative 3D structured illumination microscopy images of human β -cells infected with granule marker NPY-EGFP and Ad-shRNA-Control (**b, c**) or Ad-shRNA-Septin5 (**d, e**) for 48 h and then immunostained with tubulin. Pseudo-color encodes the depth. Color corresponds to the depth from the coverslip surface, with red being closest to the

PM surface and Cyan being in cell interior. **b** 3D reconstructed Super-resolution imaging shows Septin5 is assembled at MT-PM contact sites (*bottom*, white arrows, higher magnification view of white dashed rectangular region) as rod and punctate structures, some granules were observed anchoring to Septin5-rich sites along the MT (*bottom*, white circles, higher magnification view of white dashed rectangular region). **c** The TIRF optical section images of 3D SIM highlighted the MT-PM contact sites of the region as the dashed box indicated in (**b**). **d** Septin5 deletion does not alter the MT meshwork or the anchoring of granules (*right*, white circles). Image is depth coded as indicated. **e** The TIRF optical section images of 3D SIM highlighted the MT-PM contact sites of the region as the dashed box indicated in (**d**). Representative results of three independent experiments.

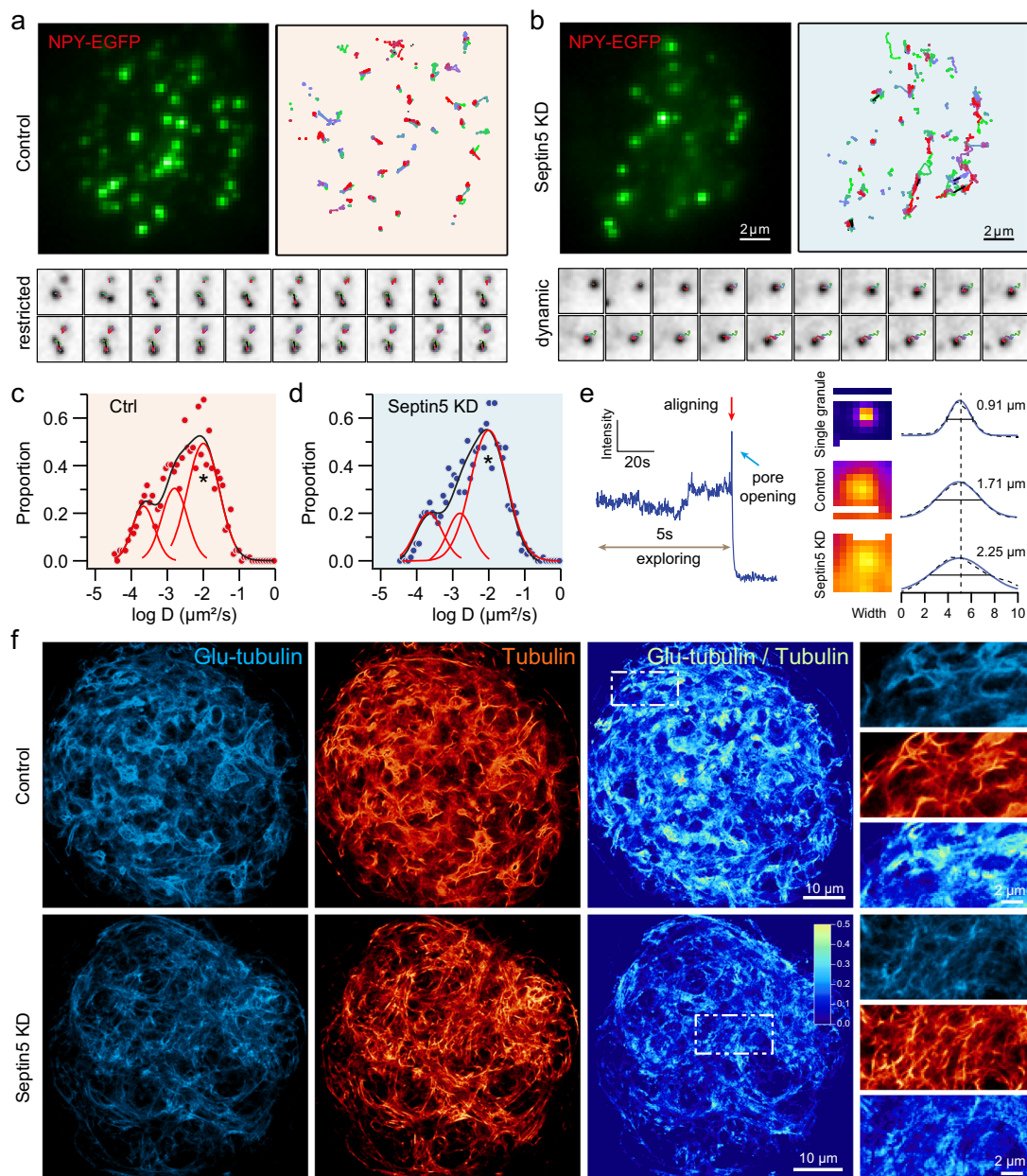
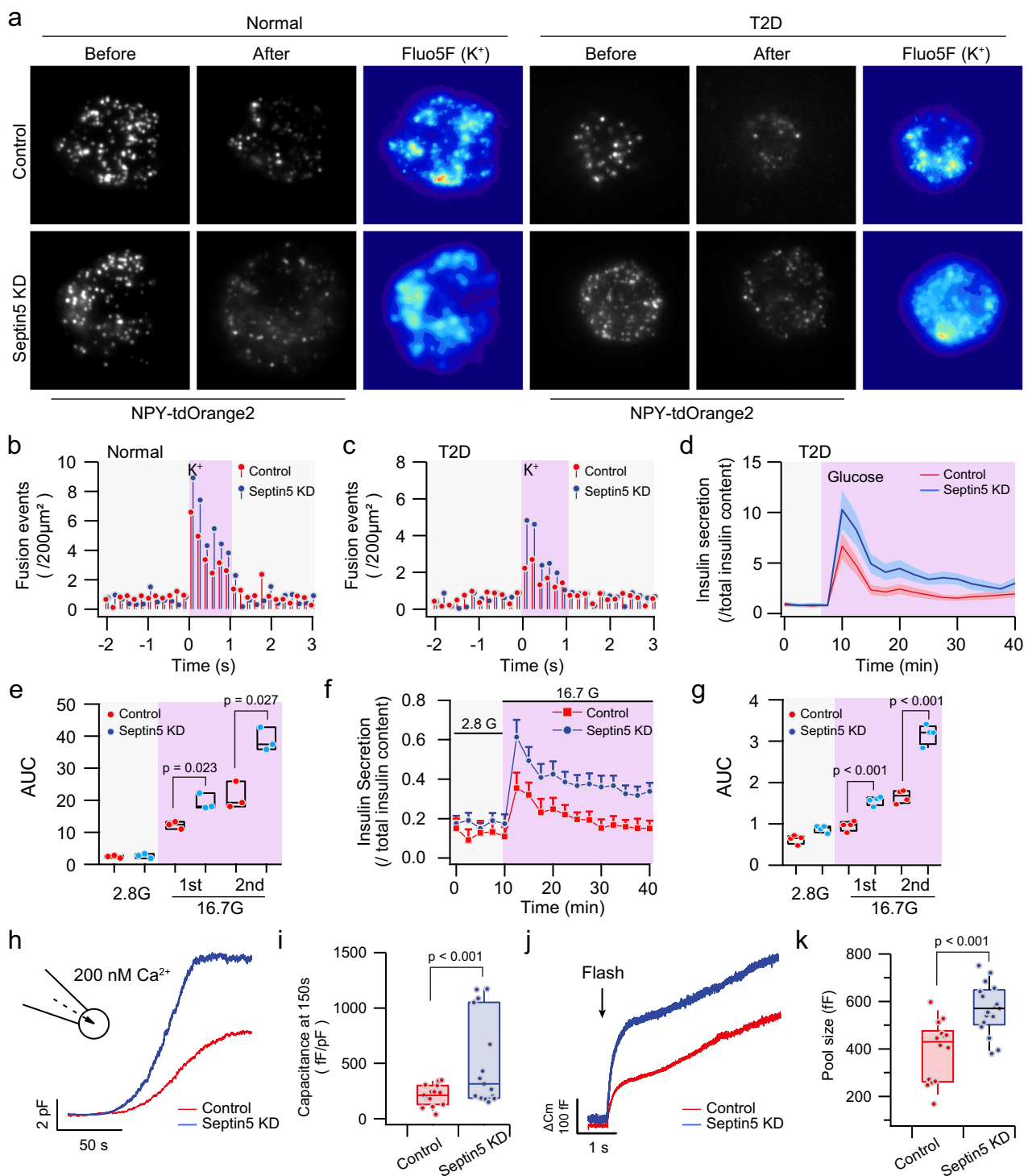


Fig. 5 | Septin5 depletion increases SGs dynamics and its access to PM and regulates MT stability. **a, b** Spatiotemporal analysis of SG dynamics during glucose stimulation in WT (**a**) and Septin5-depleted (**b**) human β -cells by TIRFM. Representative TIRFM images (*left*), sum of SG trajectories (*right*), and time-lapse images of typical SG dynamics before fusion (*bottom*). **c, d** Histogram of the granule diffusion coefficient D measured from the trajectory of individual granules in WT (**c**) and Septin5 knockdown (**d**) human β -cell after glucose stimulation. Diffusion coefficient D is a measure of how constrained diffusion of the particles, smaller values indicate more restricted movement. The raw data (dots) are fitted with a three-component Gaussian function (red line), corresponding to the nearly immobile, restricted and highly dynamic SG population, respectively (from *left* to *right*). $n = 6$ cells, ~ 700 trajectories analyzed. **e** The spatial profile of SGs “exploring” the PM before fusion showed that Septin5 depletion increases SGs access to PM. To visualize the “exploring” region before fusion, time-lapse images of ~ 70 fusion

events spatially aligned by the center coordinates of fusion site within a window of size 9×9 pixels were temporally averaged during the 5-s preceding fusion pore opening (aligning point illustrated on *left*). Spatial profiles of the average signal of NPY-EGFP at fusion sites showed in *middle*, single-granule profile included as reference. Dashed lines represent raw data, and the histogram was fitted with Gaussian function (*right*). Width, FWHM. **f** Septin5 depletion decreased the stability of MT after high glucose stimulation as indicated by the ratio (*fire*) of glu-tubulin (*turquoise*) to total tubulin (*vermillion*). The higher magnification (*right*) of regions as the dashed box (*left*) indicated showed example of region with decreased MT stability (*bottom*) compared to control (*top*). Representative images of human islets treated with high glucose for 30 min and then stained for stable MT marker, Glu-tubulin and total MT marker tubulin ($n = 3$ independent experiments, quantitative analysis of the experiments shown in Supplementary Fig. 6).

occurring at sites of Ca^{2+} entry during K^+ depolarization in human normal donor (ND) versus T2D β -cells (Fig. 6a, b). On average, 5.24 ± 0.789 granules/ $100 \mu\text{m}^2$ underwent exocytosis in response to K^+ depolarization in Septin5 depleted human β -cells, which is more than

untreated normal β -cells (3.50 ± 0.610 granules/ $100 \mu\text{m}^2$), with few events observed during the depolarization interval. In human T2D β -cells, Septin5 depletion increased the number of granules associated with L-type Ca^{2+} channels (2.61 ± 0.547 granules/ $100 \mu\text{m}^2$) by 61.1%



compared to untreated T2D β -cells (1.62 ± 0.230 granules/ $100 \mu\text{m}^2$) without affecting the number of Ca^{2+} channels and docked granules (Supplementary Fig. 7). Altogether, these results suggested that the increased granule motion and travel increase the tendency for granule fusion; and that the impaired coupling of exocytosis from sites of Ca^{2+} entry could be rescued even in T2D β -cells. This increase in SG exocytotic efficiency would be expected to culminate in improved biphasic GSIS in both T2D human islets (Fig. 6d, e) and T2D GK rat islets (Fig. 6f, g) after Septin5 depletion. The improved co-localization of granules and Ca^{2+} channels during stimulated secretion would be

expected to increase formation of excitosomes, which is a protein complex of SNARE proteins and calcium channels⁵¹. This was indeed the case, whereby after Septin5 deletion (Supplementary Fig. 8a, b) of INS-1 cells (β -cell surrogate that has more protein than islets allowing immunoprecipitation assays), glucose stimulation resulted in increased Stx3 (for newcomer SG fusion)^{22,23} and Stx1a (for predocked SG fusion) SNARE complex formation with $\text{Ca}_v1.3$ (Supplementary Fig. 8b–e).

We then assessed whether the increased excitosome formation caused by Septin5 deletion could affect Ca^{2+} sensitivity of SG fusion

Fig. 6 | Septin5 depletion increases the number of granules associated with L-type Ca^{2+} channels and increases the Ca^{2+} sensitivity of granule fusion.

a Normal and T2D human β -cell infected with granule marker NPY-tdOrange2 and loaded with Ca^{2+} sensor 2 μM Fluo5F as well as EGTA-AM stimulated with high K^+ (75 mM). The localized Fluo5F signal indicated the Ca^{2+} influx sites after depolarization. **b, c** Fusion events of granules associated with L-type Ca^{2+} channels in human normal (**b**) and T2D (**c**) β -cells. **d, e** Septin5 depletion improves GSIS in human T2D islets. The corresponding area-under-the-curve (AUC) analysis was summarized in (**e**) (Data from $n = 3$ biologically independent experiments were represented as mean \pm SEM). **f–g** The glucose-stimulated insulin secretion of GK rat islets is assessed by perfusion. 25 islets exposed to 2.8 mM glucose for 10 min, followed by 16.7 mM glucose for 30 min, during which the sample collected every 2.5 min. The corresponding AUC analysis was summarized in (**g**) (Data from $n = 3$ biologically independent experiments were represented as mean \pm SEM).

h–k Septin5 deletion increases Ca^{2+} sensitivity to both low (**h, i**) and high (**j, k**)

calcium concentrations but did not cause any change in calcium channel opening or density (Supplementary Fig. 8f, g). **h** The whole-cell capacitance change recorded during direct application of 200 nM free Ca^{2+} via patch pipette into human β -cells. **i** The average capacitance increments in control and Septin5 KD cells at 150 s following initiation of Ca^{2+} infusion and normalized to initial cell size. **j** Exocytosis was elicited by flash photolysis and monitored by whole-cell membrane capacitance measurement. Averaged capacitance changes from control (black, $n = 11$) and Septin5 KD (gray, $n = 11$) cells. Arrow indicates the flash time. **k** Averaged amplitudes of the highly calcium-sensitive pool from control (black) and Septin5 KD (white) cells respectively ($n = 11$ from three independent experiments). Statistical significance was assessed by a two-tailed Student's *t*-test (the precise statistical results indicated in figures). For boxplots, boxes indicate 25th and 75th percentiles, the lines within boxes mark medians, whiskers above and below boxes indicate the 90th and 10th percentiles. Source data are provided as a Source Data file.

by performing whole-cell capacitance measurement (C_m) recording. We first dialyzed 200 nM free Ca^{2+} via patch pipette to test low-level Ca^{2+} -dependent exocytosis (Fig. 6h, i), which showed that Septin5 deletion increased exocytosis by 141% (Septin5-KD: 508 ± 104 fF/pF; control: 211 ± 23 fF/pF). We employed a second strategy of flash photolysis of caged Ca^{2+} to induce a step-like and homogenous increase of Ca^{2+} capable of raising intracellular Ca^{2+} concentration [Ca^{2+}_i] to a high level of 2–5 μM (Fig. 6j, k). Here, right after the flash spike, there is a fast component that releases earlier than the readily releasable pool, named the highly calcium sensitive pool. Through curve fitting analysis of the first component of the C_m increase occurring during the flash photolysis, deletion of Septin5 changed the kinetics of the secretory response, showing an increase of 45% of the C_m size (Septin5-KD: 568 ± 26 fF; control: 392 ± 34 fF). The current-voltage relationship of Ca_v s in human β -cells showed that deletion of Septin5 did not change Ca_v current or density (Supplementary Fig. 8f, g), consistent with the imaging results in Supplementary Fig. 7. Taken together, Septin5 deletion increases the Ca^{2+} sensitivity for insulin SG exocytosis, suggesting Septin5 might be also act as a fusion clamp or brake in addition to serving as anchor sites for newcomer SGs and Ca_v s.

Discussion

In summary, we comprehensively demonstrated the role of Septin5 in insulin secretion in vivo, ex vivo, and in vitro by independent analyses. First, in Septin5 knock-out mice, improved glucose tolerance was shown by IPGTT and IPITT. Second, human islets depleted of Septin5 showed increase in GSIS from perfused islets as a result of increased recruitment and exocytotic fusion of newcomer insulin granules in individual human β -cells as shown by TIRFM imaging. Third, we demonstrated the mechanism by super-resolution structured illumination imaging, which revealed that Septin5 is preferentially assembled at MT-PM contact sites where insulin SGs could anchor, which when depleted, results in an increased instability of MT upon glucose stimulation leading to increased insulin SG mobilization to PM calcium channels.

Whereas the notion that the actin cytoskeleton regulates insulin secretion in pancreatic β -cells through remodeling had long been postulated³⁸, only very recent progress using high-resolution cryo-electron tomography revealed that the dynamic actin remodeling occurs at nanoscale of 12–13 nm during glucose-stimulated insulin secretion⁵². Previous studies on the roles of MT in insulin secretion have clarified the ambiguous description that MT instability increases secretion by deciphering the well-orchestrated contributions between interior and cortical MT meshwork to control the proximity of insulin granules to the PM and their anchoring onto docking receptors^{27–29,37,53}. A pool of MT-detached granules was identified to be available for subsequent docking and secretion induced by local cortical MT

depolymerization²⁸. Consistent with that report, we demonstrated that the decreased stability of cortical MT induced by Septin5 depletion increased the number of detached granules from MT and subsequently made granules more dynamic to explore expanded regions for docking sites. The dense MT network-dependent transportation (including delivery and withdrawal) of granules to PM tightly collaborates with glucose-driven MT destabilization to control the availability of detached granules from MT to docking sites²⁸. Attributed to its filamentous appearance and association with actin and MT, the highly conserved septins have been recognized as the fourth component of the cytoskeleton². Septins have been reported to be associated with MT and regulate the nucleation, organization, dynamics and post-translational modifications of MT, and even MT-dependent granule transport⁵⁴. Here we show that, Septin5 depletion influences MT stability and subsequent granule release to docking sites (Fig. 5) without affecting the overall density of the MT meshwork (Fig. 4). An explanation is that Septin5, as an MT-binding protein, could regulate local MT dynamics. Further studies are required to show whether this is by direct effect or not, given the fact that its group mate, Septin2, had been shown to direct MT directionality by affecting the MT catastrophe and MT growth²⁴.

Our results in pancreatic β -cells, taken together with its previously reported role in neurons^{13,14}, showed Septin5 depletion releases both large dense-core insulin-containing and small clear synaptic vesicles towards PM-bound calcium channel sites where exocytosis predominantly occurs in both cell types. Whereas secretion in β -cells in response to elevated glucose lasts for tens of minutes in a biphasic fashion, neuronal secretion is typically triggered by action potentials and undergoes an extremely rapid process in milliseconds. Several possibilities could explain the role of Septin5 in rapid secretory response over timescales from milliseconds to minutes: serving as a switch for the common SNAREs shared by both cell types or as a controller of a bottleneck that can continuously deliver newcomer SGs to a readily-release state. Septin5-dependent MT dynamics serving to control the timing and access of SGs to docking receptors would be more plausible since it can be exquisitely regulated by both glucose metabolism (β -cells) and Ca^{2+} influx (both β -cells and neurons) triggered by action potentials^{27,55}. Surprisingly, Septin5 depletion could also rescue the deficient GSIS in T2D GK rat islets (Fig. 6f, g) which was shown to be in part attributed to depletion of the SNARE exocytotic machinery¹⁹, further supporting our notion that Septin5 acts as a controller to limit the number of insulin granules available for secretion. Further work using the multimodal imaging methods by combining fluorescent super-resolution microscopy and cryo-electron tomography could be much more useful to decipher the mechanisms underlying Septin5's specific recruitment at the sites of MT-PM contact and even directly visualize how Septin5 couples MT instability to granule secretion.

Methods

Animals and human samples

All animal procedures and use of human pancreas were carried out in accordance with ethical guidelines of the University of Toronto's Animal Care Committee and Research Ethics Board of the University Health Network, Toronto, ON, Canada, and with approved IRBs. Animals were cared for and housed in the animal facility at The Division of Comparative Medicine (DCM), University of Toronto in accordance with the Canadian Council on Animal Care Standards and the Animals for Research Act of Ontario. Animals were maintained on a 12 h light/dark cycle at constant ambient temperature (22–23 °C) and fed standard chow and water ad libitum with nesting materials. Septin5 KO mice were previously reported by W. S. Trimble (Hospital for Sick Children, Toronto, ON, Canada)¹⁸. The GK rat, original obtained from Karolinska Institute, Stockholm, Sweden and age-matched male Wistar (Charles River) were studied. Diabetes was confirmed at 8–10 weeks of age in the GK rats. Human islets were isolated and provided by Islet-Core (P. MacDonald) of the University of Alberta, Canada, which were from institutional review board-approved donors with preoperative written informed consent for research by donors themselves and their family; the basic information is listed in Supplementary Table 1.

Antibodies and reagents

Septin5 (catalog 11631-1-AP) and actin (catalog 66009-1-Ig) antibodies were from Proteintech Group (Rosemont, IL, USA); tubulin antibody (catalog 11H10) was from Cell Signaling (Danvers, MA, USA); STX-1A (catalog SAB5600255) and insulin (catalog SAB4200691) antibodies were from Sigma-Aldrich (St. Louis, MO, USA); Munc18a antibody (catalog 610336) was from BD Transduction Laboratories (NULL, USA); SNAP25 antibody (catalog 111 011) was from Synaptic Systems GmbH (Goettingen, Germany). As gifts, Septin5 shRNA plasmid was from W. S. Trimble (Hospital for Sick Children, Toronto, ON, Canada); VAMP2 antibody was from A. Lowe (Stanford University, Stanford, California, USA), and VAMP8 antibody was from W. Hong (Institute of Molecular and Cell Biology, Singapore). FITC (catalog 711900) and Texas Red (catalog A6399) were from Thermo Fisher Scientific (Waltham, MA, USA). All other chemicals, unless specified, were obtained from Sigma-Aldrich.

TIRF and structured illumination microscopy imaging

The exocytosis study was performed with a Nikon TIRF microscopy system with a numerical aperture 1.49 and 60x objective lens as previously reported^{56–58}. To assess exocytosis, a monolayer of β -cells was infected with Ad-NPY-EGFP and cultured for 48 h before imaging. Fusion events, indicated by abrupt brightening of NPY-EGFP fluorescence, were manually selected, analyzed and categorized into predocked (docked on the PM at basal, then fuses after stimulation) and newcomer SGs (not predocked on PM at basal, then recruited to fuse with PM with little to no resident time on the PM)^{21,51,56}. SR-SIM imaging was performed with Zeiss Elyra microscopy system equipped with a 100x oil NA 1.46 objective and Andor iX3 885 detector as reported recently⁵¹. Human β -cells (control and Septin5 KD conditions) were stimulated with 16.7 mM glucose for 10 min and then fixed. Images were acquired with Zeiss Zen 2012. Reconstruction of super-resolved SIM images was performed by Zen Black software (Zeiss, Germany) using a theoretically estimated optical transfer function (OTF) and standard Wiener filtering. Each SIM image was reconstructed from 25 images in total, i.e., 5 grid orientations with 5 phases. 3 sequential images averaging is applied to reduce random noise. The contrast of all images was enhanced by linear adjustments.

Lightning confocal microscopy

This was performed as previously described^{59,60} using indicated primary antibodies at 1:200 dilution and corresponding secondary antibodies. Immunostained whole islets mounted on glass coverslips were

examined using a Leica SP8 Lightning inverted fluorescence microscope containing a Stellaris 5 confocal scan head and 4x high-performance power HyD detectors. Data acquisition and analysis were performed using LAS X software. All images were deconvoluted to remove background noise.

Morphology and immunohistochemistry

After fixation in 4% paraformaldehyde, pancreases from control and transgenic mice were fixed for 24 h in 10% buffered formalin and embedded in paraffin. The slices after hematoxylin and eosin staining and antibodies incubation were visualized with a digital microscope (Olympus, Japan). Morphometric analysis performed by quantifying mean number of pancreatic islets and mean islet area.

IPGTT, ITT and GSIS

IPGTT and ITT were performed as previously described^{21,51}. IPGTT (2 g glucose/kg BW) was performed after an 18 h fast. The mice were gently restrained without anesthesia for blood collection from the tail vein for glucose determination by glucose strips and insulin determination by RIA (EMD Millipore). ITT was conducted by i.p. injection of human biosynthetic insulin (1 U/kg BW, Eli Lilly Canada Inc.) into mice after a 6-hour fast; a drop of blood obtained from the tail vein at the indicated times was used for glucose determination. Perfusion assays on mouse pancreatic islets (50–70 islets *per* chamber) were performed as previously reported to assess biphasic GSIS^{21,51}. Insulin secretion was determined by RIA. AUC was determined above basal levels.

Flash photolysis of caged Ca^{2+} and Cm measurement

Standard bath solution for flash photolysis experiments contained (in mM): 138 NaCl, 5.6 KCl, 1.2 MgCl₂, 2.6 CaCl₂, 5 glucose, 5 HEPES (pH 7.4 with NaOH). Intracellular solution for flash experiments (in mM): 112 Cs-glutamate, 5 NP-EGTA, 3.7 CaCl₂, 2 Mg-ATP, 0.3 Na₂-GTP and 0.2 Mag-fura-2 (pH 7.2 with CsOH). NP-EGTA and Mag-fura-2 were purchased from Life Technologies (Carlsbad, CA). $[\text{Ca}^{2+}]_i$ was measured using Mag-fura-2 dye, which was excited with UV illumination alternated between 340 and 380 nm using a monochromator-based system TILL polychrome 5000 (TILL Photonics GmbH, Germany). The ratio of the fluorescent signals was converted to $[\text{Ca}^{2+}]_i$ using an *in vivo* calibration curve. To obtain stepwise increase in $[\text{Ca}^{2+}]_i$, short flashes of UV light from a xenon arc flash lamp (Rapp Optoelectronics GmbH, Germany) were applied to the whole cell. Cm was measured using an EPC-10 patch-clamp amplifier (HEKA, Lambrecht, Germany) controlled by the lock-in module of PULSE software. The capacitance traces were imported to IGOR Pro (WaveMetrics, Lake Oswego, Oregon) to analyze.

Reporting summary

Further information on research design is available in the Nature Portfolio Reporting Summary linked to this article.

Data availability

The authors declare that all data supporting the findings of this study are available within the paper and/or the Supplementary Information. Source data are provided with this paper.

References

- Hartwell, L. H., Culotti, J., Pringle, J. R. & Reid, B. J. Genetic control of the cell division cycle in yeast. *Science* **183**, 46–51 (1974).
- Mostowy, S. & Cossart, P. Septins: the fourth component of the cytoskeleton. *Nat. Rev. Mol. Cell Biol.* **13**, 183–194 (2012).
- Hartwell, L. H., Culotti, J. & Reid, B. Genetic control of the cell-division cycle in yeast. I. Detection of mutants. *Proc. Natl Acad. Sci. USA* **66**, 352–359 (1970).
- Versele, M. & Thorner, J. Some assembly required: yeast septins provide the instruction manual. *Trends cell Biol.* **15**, 414–424 (2005).

5. Surka, M. C., Tsang, C. W. & Trimble, W. S. The mammalian septin MSF localizes with microtubules and is required for completion of cytokinesis. *Mol. Biol. Cell* **13**, 3532–3545 (2002).
6. Joo, E., Surka, M. C. & Trimble, W. S. Mammalian SEPT2 is required for scaffolding nonmuscle myosin II and its kinases. *Dev. Cell* **13**, 677–690 (2007).
7. Estey, M. P., Di Ciano-Oliveira, C., Frøese, C. D., Bejide, M. T. & Trimble, W. S. Distinct roles of septins in cytokinesis: SEPT9 mediates midbody abscission. *J. Cell Biol.* **191**, 741–749 (2010).
8. Estey, M. P., Kim, M. S. & Trimble, W. S. Septins. *Curr. Biol.* **21**, R384–R387 (2011).
9. Luedeke, C. et al. Septin-dependent compartmentalization of the endoplasmic reticulum during yeast polarized growth. *J. Cell Biol.* **169**, 897–908 (2005).
10. Hu, Q. et al. A septin diffusion barrier at the base of the primary cilium maintains ciliary membrane protein distribution. *Science* **329**, 436–439 (2010).
11. Caltagarone, J., Rhodes, J., Honer, W. G. & Bowser, R. Localization of a novel septin protein, hCDCrel-1, in neurons of human brain. *Neuroreport* **9**, 2907–2912 (1998).
12. Kinoshita, A., Noda, M. & Kinoshita, M. Differential localization of septins in the mouse brain. *J. Comp. Neurol.* **428**, 223–239 (2000).
13. Peng, X. R., Jia, Z., Zhang, Y., Ware, J. & Trimble, W. S. The septin CDCrel-1 is dispensable for normal development and neurotransmitter release. *Mol. Cell Biol.* **22**, 378–387 (2002).
14. Beites, C. L., Xie, H., Bowser, R. & Trimble, W. S. The septin CDCrel-1 binds syntaxin and inhibits exocytosis. *Nat. Neurosci.* **2**, 434–439 (1999).
15. Macara, I. G. et al. Mammalian septins nomenclature. *Mol. Biol. Cell* **13**, 4111–4113 (2002).
16. Beites, C. L., Campbell, K. A. & Trimble, W. S. The septin Sept5/CDCrel-1 competes with alpha-SNAP for binding to the SNARE complex. *Biochem J.* **385**, 347–353 (2005).
17. Capurso, G. et al. Peanut-like 1 (septin 5) gene expression in normal and neoplastic human endocrine pancreas. *Neuroendocrinology* **81**, 311–321 (2005).
18. Yang, Y. M. et al. Septins regulate developmental switching from microdomain to nanodomain coupling of Ca²⁺ influx to neurotransmitter release at a central synapse. *Neuron* **67**, 100–115 (2010).
19. Ostenson, C. G. & Efendic, S. Islet gene expression and function in type 2 diabetes; studies in the Goto-Kakizaki rat and humans. *Diab. Obes. Metab.* **9**, 180–186 (2007).
20. Xie, L., Zhu, D. & Gaisano, H. Y. Role of mammalian homologue of *Caenorhabditis elegans* unc-13-1 (Munc13-1) in the recruitment of newcomer insulin granules in both first and second phases of glucose-stimulated insulin secretion in mouse islets. *Diabetologia* **55**, 2693–2702 (2012).
21. Zhu, D. et al. Dual role of VAMP8 in regulating insulin exocytosis and islet beta cell growth. *Cell Metab.* **16**, 238–249 (2012).
22. Gaisano, H. Y. Here come the newcomer granules, better late than never. *Trends Endocrinol. Metab. TEM* **25**, 381–388 (2014).
23. Spiliotis, E. T. Spatial effects—site-specific regulation of actin and microtubule organization by septin GTPases. *J. Cell Sci.* **131**, jcs207555 (2018).
24. Bowen, J. R., Hwang, D., Bai, X., Roy, D. & Spiliotis, E. T. Septin GTPases spatially guide microtubule organization and plus end dynamics in polarizing epithelia. *J. Cell Biol.* **194**, 187–197 (2011).
25. Kremer, B. E., Haystead, T. & Macara, I. G. Mammalian septins regulate microtubule stability through interaction with the microtubule-binding protein MAP4. *Mol. Biol. Cell* **16**, 4648–4659 (2005).
26. Spiliotis, E. T., Hunt, S. J., Hu, Q., Kinoshita, M. & Nelson, W. J. Epithelial polarity requires septin coupling of vesicle transport to polyglutamylated microtubules. *J. Cell Biol.* **180**, 295–303 (2008).
27. Ho, K. H. et al. Glucose regulates microtubule disassembly and the dose of insulin secretion via tau phosphorylation. *Diabetes* **69**, 1936–1947 (2020).
28. Zhu, X. et al. Microtubules negatively regulate insulin secretion in pancreatic beta cells. *Dev. Cell* **34**, 656–668 (2015).
29. Bracey, K. M. et al. Microtubules regulate localization and availability of insulin granules in pancreatic beta cells. *Biophys. J.* **118**, 193–206 (2020).
30. Trogden, K. P. et al. Microtubules regulate pancreatic β -cell heterogeneity via spatiotemporal control of insulin secretion hot spots. *eLife* **10**, e59912 (2021).
31. Kang, F. et al. E-syt1 re-arranges STIM1 clusters to stabilize ring-shaped ER-PM contact sites and accelerate Ca²⁺ store replenishment. *Sci. Rep.* **9**, 3975 (2019).
32. Giordano, F. et al. PI(4,5)P(2)-dependent and Ca²⁺-regulated ER-PM interactions mediated by the extended synaptotagmins. *Cell* **153**, 1494–1509 (2013).
33. Gong, B., Johnston, J. D., Thiernicke, A., de Marco, A. & Meyer, T. Endoplasmic reticulum–plasma membrane contact gradients direct cell migration. *Nature* **631**, 415–423 (2024).
34. Chen, Y. J., Quintanilla, C. G. & Liou, J. Recent insights into mammalian ER-PM junctions. *Curr. Opin. Cell Biol.* **57**, 99–105 (2019).
35. Hou, J. C., Min, L. & Pessin, J. E. Insulin granule biogenesis, trafficking and exocytosis. *Vitam. Horm.* **80**, 473–506 (2009).
36. Scorrano, L. et al. Coming together to define membrane contact sites. *Nat. Commun.* **10**, 1287 (2019).
37. Hoboth, P. et al. Aged insulin granules display reduced microtubule-dependent mobility and are disposed within actin-positive multigranular bodies. *Proc. Natl Acad. Sci. USA* **112**, E667–E676 (2015).
38. Orci, L., Gabbay, K. H. & Malaisse, W. J. Pancreatic beta-cell web: its possible role in insulin secretion. *Science* **175**, 1128–1130 (1972).
39. Wang, Z. & Thurmond, D. C. Mechanisms of biphasic insulin-granule exocytosis—roles of the cytoskeleton, small GTPases and SNARE proteins. *J. Cell Sci.* **122**, 893–903 (2009).
40. Yuan, T. et al. Diacylglycerol guides the hopping of clathrin-coated pits along microtubules for exo-endocytosis coupling. *Dev. Cell* **35**, 120–130 (2015).
41. Kreis, T. E. Microtubules containing deetyrosinated tubulin are less dynamic. *EMBO J.* **6**, 2597–2606 (1987).
42. Degtyar, V. E., Allersma, M. W., Axelrod, D. & Holz, R. W. Increased motion and travel, rather than stable docking, characterize the last moments before secretory granule fusion. *Proc. Natl Acad. Sci. USA* **104**, 15929–15934 (2007).
43. Atlas, D. Functional and physical coupling of voltage-sensitive calcium channels with exocytotic proteins: ramifications for the secretion mechanism. *J. Neurochem* **77**, 972–985 (2001).
44. Hao, M. et al. Regulation of two insulin granule populations within the reserve pool by distinct calcium sources. *J. Cell Sci.* **118**, 5873–5884 (2005).
45. Lou, X., Scheuss, V. & Schneggenburger, R. Allosteric modulation of the presynaptic Ca²⁺ sensor for vesicle fusion. *Nature* **435**, 497–501 (2005).
46. Hoppa, M. B. et al. Chronic palmitate exposure inhibits insulin secretion by dissociation of Ca²⁺ channels from secretory granules. *Cell Metab.* **10**, 455–465 (2009).
47. Gandasi, N. R. et al. Ca²⁺ channel clustering with insulin-containing granules is disturbed in type 2 diabetes. *J. Clin. Investig.* **127**, 2353–2364 (2017).
48. Willenborg, M. et al. Ca²⁺-dependent desensitization of insulin secretion by strong potassium depolarization. *Am. J. Physiol. Endocrinol. Metab.* **303**, E223–E233 (2012).
49. Wu, M. M., Buchanan, J., Luik, R. M. & Lewis, R. S. Ca²⁺ store depletion causes STIM1 to accumulate in ER regions closely associated with the plasma membrane. *J. Cell Biol.* **174**, 803–813 (2006).

50. Pertusa, J. A., Sanchez-Andres, J. V., Martín, F. & Soria, B. Effects of calcium buffering on glucose-induced insulin release in mouse pancreatic islets: an approximation to the calcium sensor. *J. Physiol.* **520**, 473–483 (1999).
51. Liang, T. et al. SNAP23 depletion enables more SNAP25/calcium channel excitosome formation to increase insulin exocytosis in type 2 diabetes. *JCI Insight* **5**, e129694 (2020).
52. Li, W. et al. In situ structure of actin remodeling during glucose-stimulated insulin secretion using cryo-electron tomography. *Nat. Commun.* **15**, 1311 (2024).
53. Trogden, K. P. et al. Microtubules regulate pancreatic beta-cell heterogeneity via spatiotemporal control of insulin secretion hot spots. *Elife* **10**, e59912 (2021).
54. Spiliotis, E. T. & Nakos, K. Cellular functions of actin- and microtubule-associated septins. *Curr. Biol.* **31**, R651–R666 (2021).
55. Gudimchuk, N. B. & McIntosh, J. R. Regulation of microtubule dynamics, mechanics and function through the growing tip. *Nat. Rev. Mol. Cell Biol.* **22**, 777–795 (2021).
56. Zhu, D. et al. Syntaxin-3 regulates newcomer insulin granule exocytosis and compound fusion in pancreatic beta cells. *Diabetologia* **56**, 359–369 (2013).
57. Kang, F. et al. Plasma membrane flipping of Syntaxin-2 regulates its inhibitory action on insulin granule exocytosis. *Nat. Commun.* **13**, 6512 (2022).
58. Kang F., Gaisano H. Y. Imaging Insulin Granule Dynamics in Human Pancreatic β -Cells Using Total Internal Reflection Fluorescence (TIRF) Microscopy. In: *Membrane Trafficking: Methods and Protocols* (ed Shen J.) (Springer US, 2022).
59. Lam, P. P. et al. Munc18b is a major mediator of insulin exocytosis in rat pancreatic beta-cells. *Diabetes* **62**, 2416–2428 (2013).
60. Xie, L. et al. Syntaxin-4 mediates exocytosis of pre-docked and newcomer insulin granules underlying biphasic glucose-stimulated insulin secretion in human pancreatic beta cells. *Diabetologia* **58**, 1250–1259 (2015).

Acknowledgements

This work was supported by a grant from Canadian Institute of Health Research (CIHR-PJT-159741 and MOP 119352) to H.Y.G. Some of the equipment used in this study was supported by the 3D (Diet, Digestive Tract and Disease) Centre funded by the Canadian Foundation for Innovation and Ontario Research Fund, project number 19442. The authors thank the Imaging Facility and SPARC Drug Discovery Core Facility, The Hospital for Sick Children, Toronto, Canada, for assistance with imaging and virus packaging.

Author contributions

F.K. conducted knockdown, GSIS, IP, TIRFM, SR-SIM and confocal imaging experiments and detailed analysis. L.X. performed patch clamp,

TIRFM, and SR-SIM imaging experiments. T.Q. and T.L. performed IPGTT and ITT experiments. T.Q. performed perfusion assay. Y.K. with H.X.'s assistance performed western blots. C.D.F. and H.X. assisted in plasmids construction. A.A. and C.M.Y. built the customized TIRFM. W.S.T. provided the Septin5 knockout mice and commented the manuscript. F.K. formulated the original hypothesis, interpreted the data and drafted the manuscript. H.Y.G. supervised the study and revised the manuscript. All authors discussed the results and contributed to the manuscript revision.

Competing interests

The authors declare no competing interests.

Additional information

Supplementary information The online version contains supplementary material available at <https://doi.org/10.1038/s41467-025-57421-5>.

Correspondence and requests for materials should be addressed to Li Xie, Fei Kang or Herbert Y. Gaisano.

Peer review information *Nature Communications* thanks the anonymous reviewer(s) for their contribution to the peer review of this work. A peer review file is available.

Reprints and permissions information is available at <http://www.nature.com/reprints>

Publisher's note Springer Nature remains neutral with regard to jurisdictional claims in published maps and institutional affiliations.

Open Access This article is licensed under a Creative Commons Attribution-NonCommercial-NoDerivatives 4.0 International License, which permits any non-commercial use, sharing, distribution and reproduction in any medium or format, as long as you give appropriate credit to the original author(s) and the source, provide a link to the Creative Commons licence, and indicate if you modified the licensed material. You do not have permission under this licence to share adapted material derived from this article or parts of it. The images or other third party material in this article are included in the article's Creative Commons licence, unless indicated otherwise in a credit line to the material. If material is not included in the article's Creative Commons licence and your intended use is not permitted by statutory regulation or exceeds the permitted use, you will need to obtain permission directly from the copyright holder. To view a copy of this licence, visit <http://creativecommons.org/licenses/by-nc-nd/4.0/>.

© The Author(s) 2025